Laboratory Investigation (2009) 89, 1063–1070

A computational approach to compare microvessel distributions in tumors following antiangiogenic treatments

Marco Righi[1,2], Arianna Giacomini[3,4], Cristiana Lavazza[3,4], Daniela Sia[3,4], Carmelo Carlo-Stella[3,4] and Alessandro M Gianni[3,4]

Experimental approaches currently used to quantify the activity of antiangiogenic treatments in cancer therapy do not generally address the importance of spatial distribution of microvessels in target tissues. We report a new computerized method to assess tumor vascularization by quantifying the distribution of functional microvessels as revealed by *in vivo* staining with sulfosuccinimidyl-6-(biotinamido) hexanoate. Our approach was based on pixel dilation of digital images of blood vessels and addressed the space-filling property of the vessel layouts. This was practically achieved computing the number of dilation cycles (Halo index) needed to permeate a pre-defined amount of each image. Our approach was validated on human tumor xenografts in nonobese diabetic/severe combined immunodeficient mice treated with the antiangiogenic drug sorafenib. For each experimental model, area normalization allowed the unbiased comparison of several hundreds of images showing different amounts of vascular tissue. In two different tumor types, comparison of Halo values showed statistically significant differences between control and sorafenib-treated samples. Conversely, this effect was not observed in samples from an additional xenograft known to resist the antiangiogenic treatment. By separating the analysis of vessel area from the quantification of vessel distributions, our approach can potentially contribute to a better evaluation of the antiangiogenic or vascular-disrupting activity of new drugs or treatments.
Laboratory Investigation (2009) **89,** 1063–1070; doi:10.1038/labinvest.2009.76; published online 3 August 2009

KEYWORDS: angiogenesis; image analysis; mathematical morphology; microvessel distribution; vascular targeted therapies

Most tumor cells rely on an intact vascular supply for their survival, making the tumor vasculature an attractive target for therapy.[1,2] Development of antiangiogenic strategies has focused on several agents, such as inhibitors of vascular endothelial growth factor[3] and inhibitors of matrix metalloproteinases,[4] now in clinical trial. In contrast to the antiangiogenic approach, vascular-disrupting therapies aim to target the established tumor vasculature, causing a rapid and extensive decrease in tumor blood flow and, thus, secondary tumor cell death.[5] These approaches demand appropriate tests to quantify the effects induced on tumor vessels. Unfortunately, this seems to be a complex task because efficient vascularization of a tissue depends not only on the number and size of functional microvessels but also on their shape and distribution.[6]

At present, high-throughput automatic instruments for digital acquisition of stained histological samples,[7] coupled with the development of improved analytical tools,[8] allow unsupervised analysis of highly vascularized hot-spots,[9] or whole tumor sections. However, although computerized approaches increase reproducibility in calculating vessels sizes and densities,[10,11] they are unable to quantify the distribution of vessels in the tissues analyzed. Efforts in this direction have involved the use of the fractal dimension (D_f)[12,13] of the samples, as a generalization of the Euclidean (integer) concept of geometrical dimension. Applying this approach to the description of planar vessel layouts,[14] Baish *et al*[15] calculated differences in the D_f of vascular trees made of arteries and veins, capillaries, or tumor vessels. Despite these successes, fractal analysis suffers from some drawbacks,

[1]Consiglio Nazionale delle Ricerche, Institute of Neuroscience, Cellular and Molecular Pharmacology Section, Milan, Italy; [2]Department of Medical Pharmacology, "E. Trabucchi", University of Milano, Milan, Italy; [3]Medical Oncology, Fondazione IRCCS Istituto Nazionale Tumori, Milan, Italy and [4]Medical Oncology, University of Milano, Milan, Italy
Correspondence: Dr M Righi, PhD, Consiglio Nazionale delle Ricerche, Institute of Neuroscience, Via Vanvitelli 32, I-20129 Milano, Italy.
E-mail: m.righi@in.cnr.it

Received 21 April 2009; revised 26 May 2009; accepted 26 May 2009

particularly when applied to non-fractal objects.[16] In any case, need for image pre-processing (eg skeletonization),[14,17] choice of an appropriate procedure (usually fractal box counting),[18] and choice of adequate assay parameters (eg set of box sizes) demand caution and experience to determine absolute D_f values.

To overcome these difficulties, we have devised a practical approach based on the space-filling property of the vessel distribution to be quantified. We calculated this value taking advantage of the mathematical morphology operator dilation[19,20] that caused image fill-up by cycles of single-pixel expansion of foreground structures (the identified vessels) according to a pre-defined scheme (the so called 'structuring element'). Assuming that slow image filling should show regions of poor vascularization, our calculation would indicate which areas are more prone to necrotic events. Application of this paradigm to the analysis of experimental tumors, receiving an antiangiogenic treatment, highlighted the effects of the drug sorafenib [21] in the disruption of tumor-associated vasculature.

MATERIALS AND METHODS

Human Tumor Xenografts

The human multiple myeloma KMS-11, the NHL-lymphoma SUDHL4-V, and the B-lymphoma JVM-2 cell lines were cultured in RPMI-1640 supplemented with 10% fetal bovine serum. All cultures were periodically tested for mycoplasma contamination. Experimental tumors were grown in NOD/SCID mice (Charles River, Milano, Italy, EU) by subcutaneous inoculation of 5×10^6 KMS-11, SUDHL4V, or JVM-2 cells (DSMZ, Braunschweig, Germany, EU). When subcutaneous nodules reached approximately 10 mm in diameter, mice received a daily intravenous injection of 60 mg/kg sorafenib[21] for 5 days. Three hours after the last treatment, tumors were excised and analyzed. Mice were housed under standard conditions according to our institutional guidelines. Animal experiments were performed according to the Italian laws (D.L. 116/92 and following additions), which enforce the EU 86/109 Directive, and were approved by the institutional Ethical Committee for Animal Experimentation.

Tumor Vascularity

To analyze tumor vasculature, proteins expressed on the luminal surface of vascular endothelium were biotinylated *in vivo*[22] by intravenous injection of 0.2 ml sulfosuccinimidyl-6-(biotinamido) hexanoate (sulpho-NHS-LC-biotin, Thermo Fisher Scientific, Rockford, IL, USA) (5 mg/ml) in polygeline. Sulfo-biotin was allowed to circulate for 5 min, and then mice were intravenously injected with 1 ml of Tris/Polygeline (50 mM) to neutralize circulating sulpho-NHS-LC-biotin. Five minutes later, tumors were excised, embedded in cryo-embedding compound, and snap-frozen in isopentane pre-cooled in liquid nitrogen for preparation of cryosections. Sections were cut at a thickness of 4 μm from randomly oriented samples to avoid variation because of the Holmes effect.[23] Tumor endothelial cells were then revealed by staining frozen sections with horseradish peroxidase-conjugated streptavidin (Dako, Glostrup, Denmark). For each experimental condition, we processed an average of three tumor nodules analyzing at least three sections.

Image Acquisition and Processing

Images of tissue sections were acquired at $\times 20$ magnification with an automatic high-resolution scanner (dotSlide System, Olympus, Tokyo, Japan) and subdivided in a collection of non-overlapping RGB images in TIFF format (final resolution 3.125 pixels/μm). Image analysis was carried out using the ImageJ software[24] version 1.40g.

To prepare samples for analysis, the dynamic range of RGB images was fully expanded by contrast enhancement, and then images segmented to identify sulpho-NHS-LC-biotin-stained cells. This was obtained by application of combined thresholds in the Hue (0–30) and Saturation (200–255) channels. After segmentation, the ImageJ command Analyze Particles was used to remove small particles up to 40 pixels. In addition, when appropriate, the Binary > Fill Holes tool was used to fill the lumen of cross-sectioned vessels.

Fractal Dimension, Permeation Curves, and Indexes of Spatial Distribution

D_f values were calculated using the FraLac plug-in (version 2.5d), in association with the ImageJ program, using the FraLac default linear series or the power series box sizes. Results were averaged over four iterations of the algorithm, each run assuming the starting point at a different corner of the image. Images were analyzed both directly and after simple skeletonization,[17] using the default built-in command of the ImageJ application.

For each image, the percent vascular area was calculated as the initial fraction of black pixels. Conversely, permeation curves were constructed by repeated pixel dilations, plotting the percent of permeated area against the number of dilation cycles needed to obtain such value. For most of the work, permeation curves were calculated alternating the square and cross structuring elements. According to which element was used for the first dilation, this procedure produced two saw-tooth curves sharing points every two dilation steps. Intermediate points were obtained by linear interpolation.

For each curve, we calculated the value of dilation cycles needed to permeate 90% of the entire image (Halo index or $H_{90\%}$). In the case of artificial distributions we also used higher percentiles (95 or 99%). For each set of images compared, we normalized Halo indexes to satisfy the following condition: 'equivalent vessel layouts with different vessel area should give the same $H_{90\%}$ index'. Our definition of equivalent vessel layout was 'layouts providing equal permeation curves by sequential dilations'. Practically, we found

the maximal vessel area observed among all images under comparison and, then, for each image, we calculated the number of dilation cycles (H_{ini}) needed to reach that value. Finally, for each image, we obtained normalized Halo values ($nH_{90\%}$) by subtraction: $nH_{90\%} = H_{90\%} - H_{ini}$. Frequency distributions of $nH_{90\%}$ values for a set of images were obtained grouping values in a set of equidimensional classes and plotting the resulting numbers. When appropriate, classes were color coded and images represented as spatial color maps on the basis of their $nH_{90\%}$ value. This approach was followed also for the percent image area covered by stained vessels and for D_f values.

Automated and Statistical Analyses

Calculations of permeation values and raw, or normalized, H indexes were performed using an ImageJ routine. This macro was developed according to the indications posted in the Developer Section of the ImageJ web site and its code is provided as Supplementary material. Correlations and statistical analysis were performed with the statistical package Prism 5 (GraphPad Software, San Diego, CA, USA). The correlation coefficient R^2 was calculated as the square of the covariance of the two variables divided by the product of their standard deviations. To test the probability of significant differences between untreated and sorafenib-treated samples, we used the Mann–Whitney non-parametric test.[25] Differences were considered significant if $P < 0.001$. This low value was used to highlight clear-cut statistic differences between non-Gaussian, non-parametric, skewed distributions of large datasets, where a little number of outlying points might have increased the statistical significance without having a significative biological importance. It must, however, be stressed that this strict condition prevents the recognition of real, small differences between close datasets, and might be not suitable for every test conditions.

RESULTS

Permeation Curves and Halo Indexes

A typical image, out of a collection obtained from a sulpho-NHS-LC-biotin-stained tumor nodule, is shown in Figure 1a

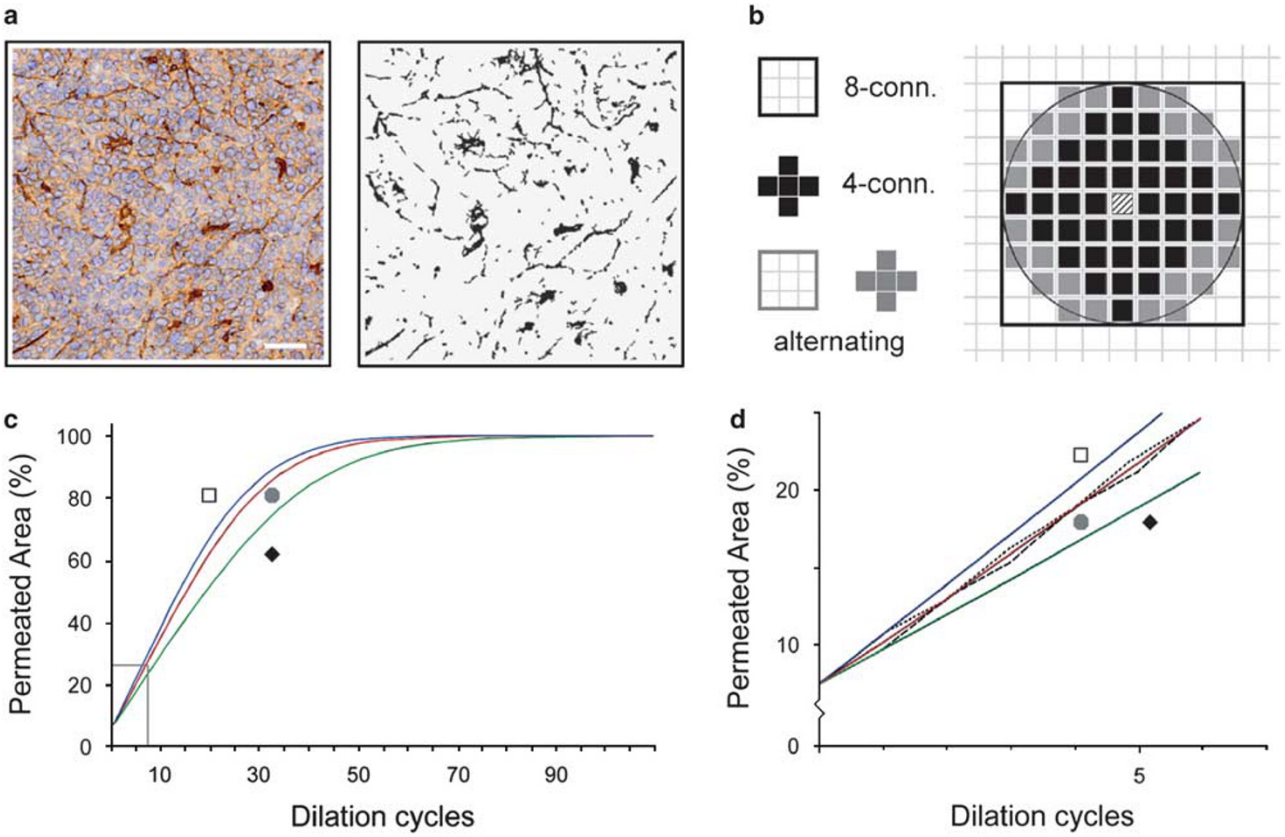

Figure 1 Permeation curves and structuring elements. (**a**) Sample RGB image, derived from scans of tumor sections stained *in vivo* with sulpho-NHS-LC-biotin, together with its relative, segmented, black and white image. Scale bar: 50 μm. (**b**) Area permeated by a single pixel (striped square) after four dilation cycles using the different structuring elements (SE) shown on the left. Use of a square SE resulted in permeation of the area delimited by a thick black border. Use of a cross SE resulted in permeation of the area represented in black. Alternate use of both SE permeated the area shown in gray. (**c**) Permeation curves of (**a**) using square (blue), cross (green), or alternating SE (red) as identified also by the geometry of the nearby symbol. The inset, delimited by gray lines, is shown magnified in (**d**) to highlight the saw-tooth curves (striped lines) obtained alternating SE as well as the resulting interpolation curve (red).

before and after vessel identification. In an ideal case, unrestricted pixel dilations should be calculated as expanding circles. Practically, however, reiterated dilations using exclusively 8-connected (square), or 4-connected (cross), structuring elements (Figure 1b) gave rise to expanding squares, either normal or tilted by 45°. In contrast, the alternated use of 4- and 8-connected elements yielded octagonal shapes that better approximated circles (see movie in Supplementary files). Convolution of our sample image, plotting permeated area fractions against dilation cycles, produced the curves shown in Figure 1c, on the basis of the structuring element used. According to which element was used for the first dilation, alternating elements generated two different saw-tooth curves (Figure 1d), which were adequately described by the interpolating curve passing through common points. From here beyond, we will use only the interpolated curve to describe tissue permeation by pixel dilations.

To quantify the efficiency of vessel distributions in generating a halo of permeated tissue we calculated the number of cycles needed to fill 90% of the area of the analyzed image and named it $H_{90\%}$, where *H* stands for 'Halo'. Analysis of different artificial distributions of an equal number of objects (Supplementary Figure 1), pointed out that higher percentile *H* indexes (eg $H_{95\%}$ or $H_{99\%}$) might be useful to identify very small changes in pixel distributions, which would otherwise not be shown. In real samples this was not the case and different vessel distributions showed different $H_{90\%}$ results with increasing values correlating with a poorer space-filling layout.

Quantification of Blood Vessel Distributions in Tumor Slices

To prepare biological samples for halo analysis, we acquired collections of squared RGB images, roughly 0.135 mm^2 in size (1.32×10^6 pixels), from histological sections of sulpho-NHS-LC-biotin-stained tumor nodules. Images containing regions devoid of living tissue (ie holes, fat drops, absence of sample) larger than 10% of the total image surface were discarded. Images showing vessels with an unfilled lumen did not influence the calculation of $H_{90\%}$ values because hollow spaces were rapidly filled by dilation of the surrounding vessel walls. This was confirmed by comparing results obtained from images before and after fill-up of vessel lumen (data not shown).

After vessel identification, we usually removed particles smaller than 40 pixels as a possible source of unwanted noise. To assess the importance of this step we analyzed up to 930 images from an untreated KMS-11 tumor xenograft observing a moderate increase in $H_{90\%}$ values after particle removal. This increment was observed on all samples and did not otherwise influence the results obtained (Supplementary Figure 2).

Finally, computation of raw $H_{90\%}$ values, using the same set of 930 images, showed a moderate, inverse dependence on the image area covered by vessels (Figure 2a). However, complete independence (normalization) of *H* indexes could be obtained through pixel dilation. For each image of a set, this step ideally deposed new pixels around those already existing, until all images showed the same amount of vascular surface, albeit differently distributed. This passage could be accomplished graphically, shifting leftwards the appropriate permeation curves or, mathematically, subtracting the number of cycles needed to equalize the amount of vascular surfaces (see Materials and Methods; Figure 2b). According to this procedure, normalization was relative, being applied only to the comparison under way and only to the images involved, but allowed unbiased evaluations of different vessel distributions.

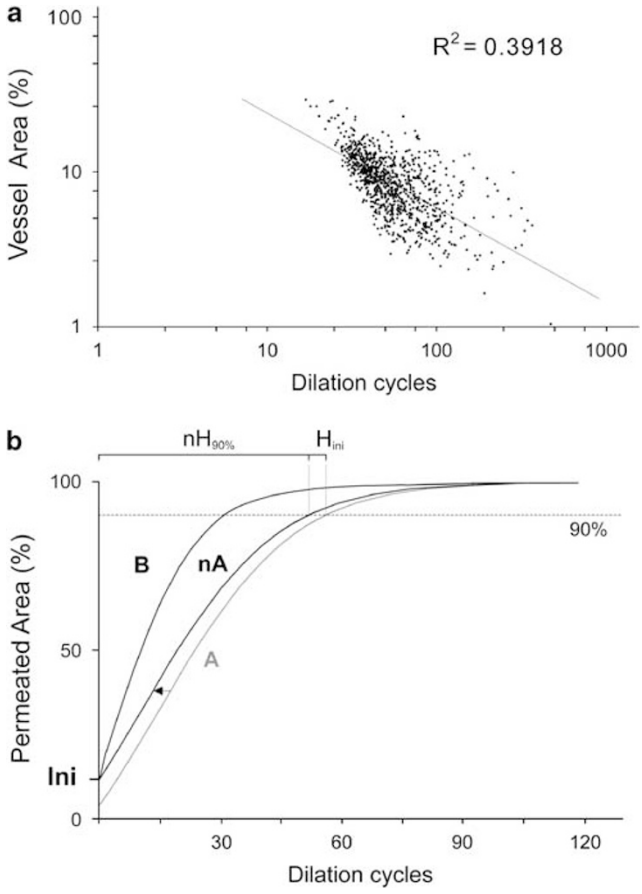

Figure 2 Dependence on surface and normalization of permeation curves. (**a**) Correlation between $H_{90\%}$ values and percent vessel area as observed in a set of 930 black and white images from sections of untreated KMS-11 xenografts. The linear correlation coefficient R^2 is reported. (**b**) Independence of *H* index on initial vessel surface was obtained by normalization. The plot shows the graphical normalization of curves (A) and (B) by a leftward shift of the curve obtained from a less vascularized image (curve A) until interception of curve (curve B) (obtained from a more vascularized image) on the *y*-axis at point Ini. The normalized $H_{90\%}$ index ($nH_{90\%}$ in the figure) could be obtained from the new curve (nA) or, mathematically, by subtracting the amplitude of the shift (H_{ini}) from the raw $H_{90\%}$ value.

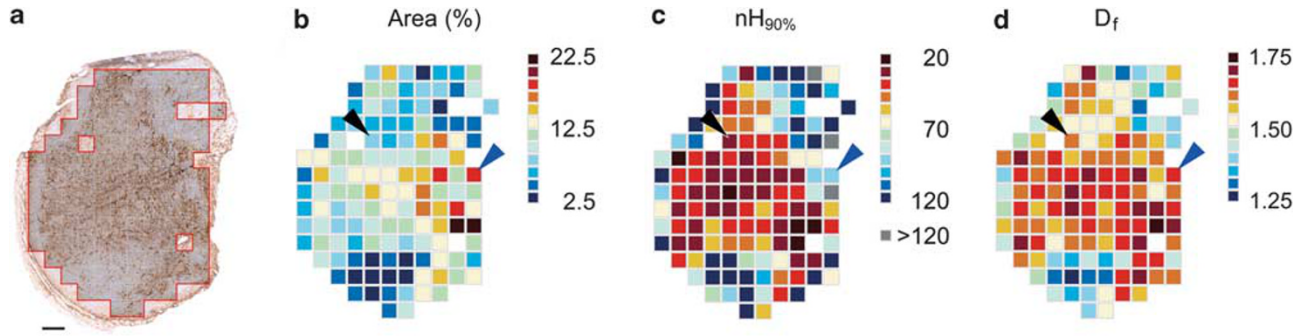

Figure 3 Spatial maps of microvascular distribution. (**a**) Low magnification image of a section from a sulpho-NHS-LC-biotin-stained tumor. A red border identifies the images used for the analysis of microvessel distribution. Scale bar 500 μm. (**b**) The color-coded map of percent vessel areas as determined on segmented, black and white images. Surface values were grouped and represented according to the color scale reported in the panel. (**c**) Representation of n$H_{90\%}$ values calculated for each image of the section. Values were grouped and coded according to the color scale shown on the right of the panel. To obtain a better visualization, three out-of-scale values (n$H_{90\%}$ >120) were shown as a separate group. Low n$H_{90\%}$ values identify images with high space-filling characteristics. (**d**) Map of D_f values, obtained on non-skeletonized images using a linear series of box sizes. Values were coded according to the color scale shown on the right of the panel. High D_f values suggest high space-filling characteristics. Black and blue arrowheads point to images with relatively divergent n$H_{90\%}$ and D_f values. Black when H index suggested a high space-filling property, blue when this property was suggested by D_f. Details of these images are reported in Supplementary Figure 4.

Mapping Area and Space-Filling Properties of Vessel Distributions on Tumor Slices

Images from a same nodular section (Figure 3a) presented variable amounts of microvasculature. These values could be expressed as percent covered area and visualized as a map, after classifying data into color-coded groups (Figure 3b). A similar approach could be carried out for the corresponding normalized H values (n$H_{90\%}$) to obtain at-a-glance summaries of microvessel distributions with specific space-filling properties. As shown in Figure 3c for a typical tumor slice, the pattern of images with low n$H_{90\%}$ values (high space-filling properties) differed from that of images showing high microvessel area.

Earlier works used the fractal dimension (D_f) of vessel layouts as an index of vessel distribution.[14,26] Although this approach is appropriate for planar models, its use is questionable when analyzing sections of a 3D vessel network, which do not show self-similarity. In these conditions, D_f is dependent on both the amount of signal and its distribution. This can be observed comparing our results with those obtained by Fractal Box Counting (Figure 3d; Supplementary Figure 3). When $H_{90\%}$ and D_f maps differed (eg black or cyan arrowheads), visual inspection suggested that D_f values were more influenced by the amount of microvasculature (Supplementary Figures 4 and 5) than by its distribution. This dependence was little affected by skeletonization or by changes in box series and reflected loss of scale-invariance in the scanned images.

Antiangiogenic Treatment Increased nH Values in Tumor Slices

To test H index for changes in vessel distribution, we used the antiangiogenic drug sorafenib known to affect tumor xenografts reducing the amount of infiltrating microvessels.[21] In this analysis, we compared 930 images from untreated controls with 936 new samples from sorafenib-treated mice, acquiring images from different sections ($n \geq 7$) coming from treated ($n = 4$) or untreated ($n = 3$) animals. All the 1866 resulting n$H_{90\%}$ values were grouped in 10 cycle-wide classes and sorted in terms of treatment. The final histograms, plotted in Figure 4a, showed higher, and more dispersed, n$H_{90\%}$ values for sorafenib-treated samples with respect to untreated tumors. This inter-group difference was highly significant in a Mann–Whitney non-parametric test with $P < 0.001$. Reproducibility of results inside a same group of data seemed excellent for controls and, to a lesser extent, for sorafenib-treated samples (Supplementary Figure 6). Reduction in space-filling characteristics was paralleled by reduction of vessel areas in images from sorafenib-treated datasets (Figure 4b), confirming the expected action of the drug ($P < 0.001$). All of these analyses were repeated on unfiltered, original images with similar results (data not shown).

Analysis of Additional Experimental Models

To establish whether our new computational method could show antiangiogenic effects in experimental models other than the KMS-11 tumor, we repeated the analysis on sorafenib-treated xenografts obtained with the JVM-2 and the SUDHL4-V cell lines. These cell lines give origin to necrotic xenografts, which are not totally suitable for analysis, thus lowering the number of processable samples to an average 270 images for each condition. Results obtained from both models were compared with those obtained from a subset of images, with close numerical consistence, from the KMS-11 set already analyzed. As can be seen (Figure 5a), in the KMS-11 and SUDHL4-V xenografts we observed a significant difference in n$H_{90\%}$ values after sorafenib treatment ($P < 0.001$). This was not the case for images from the JVM-2

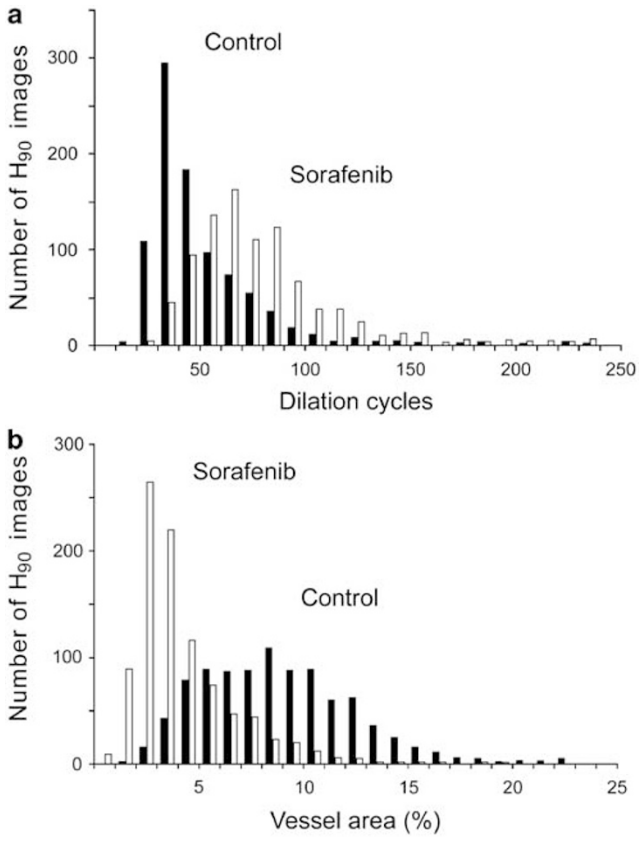

Figure 4 Changes in space-filling and area values after antiangiogenic treatment in KMS-11 samples. (**a**) Distribution of n$H_{90\%}$ values, classified in 10 cycle-wide groups, for untreated ($n = 930$, closed bars) and sorafenib-treated ($n = 936$, open bars) images. Height of bars refers to the total number of images showing an n$H_{90\%}$ value belonging to a given class. Normalization was carried out for all images against the sample showing maximal vessel area. (**b**) Distribution of initial percent areas within each set of images, before normalization. Values were binned in 1% groups.

model that showed no significant increase in H values, or reduction in vessel area. This was also suggested by tumor sizes, which did not differ from controls after sorafenib treatment. In contrast, in susceptible tumors, changes in vessel layouts were paralleled by a drop in the surface of the identified vessels (Figure 5b), confirming the action of the antiangiogenic treatment on both the amount of vessels and their space-filling properties.

DISCUSSION

In this paper, we describe a computational method to quantify microvessel distributions in tumor sections on the basis of their space-filling property. Our approach was based on the mathematical morphology operator dilation[20] and was aimed at quantifying, in the absence of human supervision, the effect of antiangiogenic treatments in experimental tumors. In this respect, we focused on microvessel distribution, in addition to total microvessel area, on the assumption that good tissue oxygenation ensues from well-distributed oxygen sources.

Our approach did not require image pre-processing other than vessel identification and removal of unsuitable sample images. However, image acquisition by transmission scanning of tumor sections implied the need for a thin, constant section thickness. This was necessary to minimize and uniform the volume of sample containing the vessels to be projected on the scanning plane. Additionally, because of the Holmes effect,[23] which would preferentially increase the area of in-plane vessels, we assumed that vessels in tumor nodules were randomly oriented.

No other assumptions were necessary. In this respect, the choice of the size of the square, used to divide tumor sections in collections of juxtaposed images, was completely arbitrary. Nevertheless, this step did not affect comparisons as long as all the input images had the same size and were similarly treated. Actually, the fact that Halo is a relative index, more than an absolute one, underscores the difference between our method and fractal-based approaches, even though pixel dilation was formerly used for the calculation of the Minkowsky–Bouligand fractal dimension.[27]

We normalized images, showing variable amounts of vessels, by virtual dilation of initial surfaces up to an equal value. Thus, we were able to obtain an unbiased estimate of the microvessel network of up to 1800 images, in a single run and without human intervention. In contrast, the finding that fractal dimension was influenced, in our samples, by the amount of signal should not be surprising. Although tumorous vessel trees can be considered scale invariant 3D structures, our thresholded 2D images of functionally stained vessels could not. This might explain why simple image skeletonization did not help in reducing the observed dependence between D_f and the image area covered by scanned vessels.

Taking advantage of our routine, in this work we confirmed the antiangiogenic effect of the drug sorafenib on xenotransplanted tumors both in terms of vessel area and vessel distribution. Thus, we propose Halo index as a new parameter, complementary to total microvessel area, to describe the relative oxygenated state of a tissue, or tumor, biopsy. The combined analysis is now able to identify differences in samples even when they present a close amount of covered vascular area.

In our approach, appropriate tissue staining and image segmentation were critical points to obtain bona fide vessel distributions. Thus, vessel identification as functional structures perfused by the blood stream[22,28] was mandatory to map sources of tissue O_2, as opposed to methods based on detection of endothelial markers.[29] Moreover, functional staining protected against possible irregularities in blood flow, which might create poorly irrorated areas despite adequate vascularization.[15] As for image segmentation, it was carried out by thresholding images represented in an HSB color space[30] followed by removal of unwanted particles.

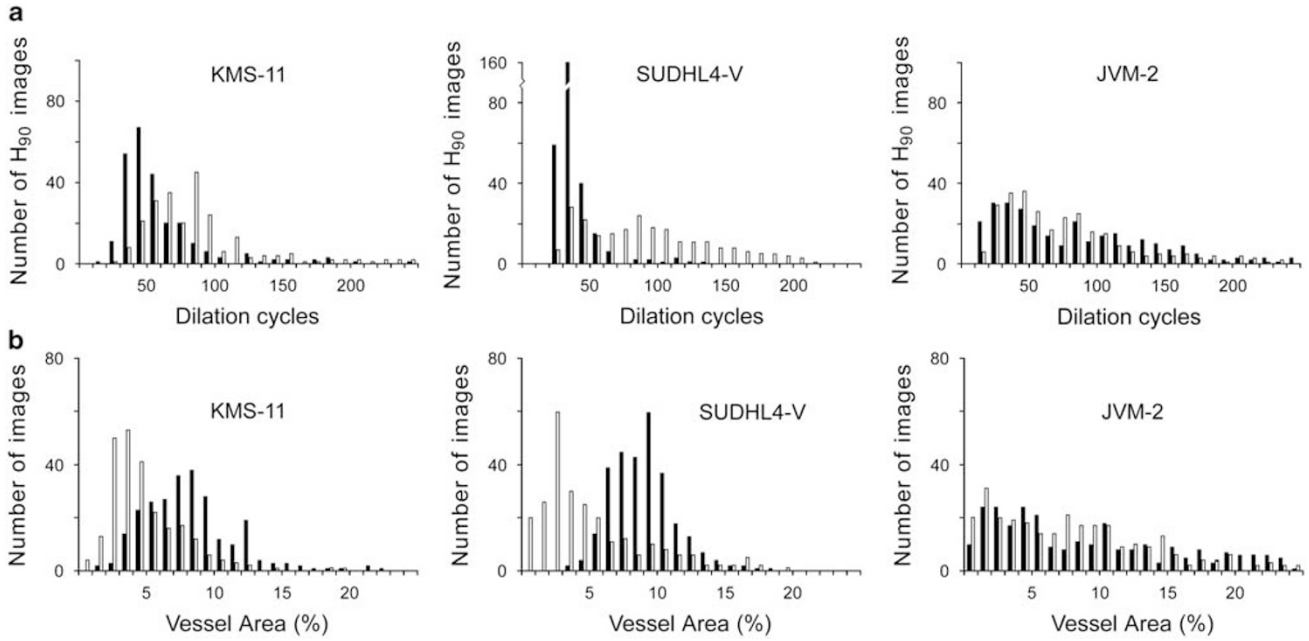

Figure 5 Characterization of antiangiogenic effects according to xenograft sensitivity. (**a**) Distribution of $nH_{90\%}$ values in three different xenografts with or without sorafenib treatment. Each histogram reports the name of the xenograft from which it was obtained. (**b**) Distribution of initial percent areas within each xenograft and set of images. Closed bars identify values from untreated samples and open bars values from sorafenib-treated tumors. The number of samples was comparable, with $n = 258$ (controls) and $n = 246$ (sorafenib) for KMS-11, $n = 292$ (controls) and $n = 255$ (sorafenib) for SUDHL4-V, $n = 287$(controls) and $n = 285$ (sorafenib) for JVM-2.

Although we found this approach satisfactory, it might be possible that other experimental models require a more refined strategy to correctly identify vascular structures. If this is the case, the use of pattern recognition algorithms[31] might contribute to solve the issue.

Despite this caveat, the possibility to quantify the space-filling property of a microvessel network provides a tool to investigate neo-angiogenic processes in physiopathological conditions. In the oncological field, we expect that the possibility to quantify separately the amounts of vessels from their space-filling arrangement might help in characterizing the antiangiogenic and vascular-disrupting potential of new drugs or treatments.[32] In a simplistic view, antiangiogenic drugs would prevent the formation of new vessels inhibiting ramification of neo-formed and well-dispersed vessels, affecting both the area and the space-filling value of tumor vessel layouts. On the other hand, the action of vascular-disrupting agents on pre-existing, and larger, capillaries should cause morphological alterations leading to changes in the distribution of functional vessels more than the reduction in endothelial area. Future investigations will be needed to verify these possibilities.

In addition to statistical analysis, topographic maps of microvessel distributions might be used to highlight areas of the tumor more prone to become necrotic (central *versus* peripheral areas), allowing a better characterization of the action of the vascular targeting agent to be studied. Besides cancer therapy, these maps might also be useful to point out spatial correlates between hypervascularized areas and histopathological features. Provided the availability of suitable mouse models, these investigations might involve Crohn's disease,[33,34] ulcerative colitis, or other inflammatory bowel pathologies.[35,36]

These future fields of investigation raise questions about the speed of analysis. Morphological dilation is a slow process, therefore a more efficient approach to compute the permeation curves would use the Euclidean Distance Map of the non-vessel fraction of the images. This algorithm was not used in this work because of practical difficulties in automating the process. However, using sequential dilations, we could analyze about a thousand images a day (about 140 mm^2) on a single computer. Although this score might seem limited, we expect that the utilization of a top hardware setup and a dedicated compiled algorithm would result in a marked increase in performance.

Supplementary Information accompanies the paper on the *Laboratory Investigation* website (http://www.laboratoryinvestigation.org)

ACKNOWLEDGEMENTS

We are indebted to E Procacci for technical assistance in slide scanning, to F Clementi for continuous support, and N. Borgese for critical revision of the manuscript. This work was supported in part by grants from CNR (Rome, Italy), Ministero dell'Istruzione, dell'Università e della Ricerca (MIUR, Rome, Italy), Ministero della Salute (Rome, Italy), and Michelangelo Foundation for Advances in Cancer Research and Treatment (Milano, Italy).

DISCLOSURE/CONFLICT OF INTEREST

The authors declare no conflict of interest.

1. Arap W, Pasqualini R, Ruoslahti E. Cancer treatment by target drug delivery to tumor vasculature in a mouse model. Science 1998;279:377–380.
2. Denekamp J. The tumor microcirculation as a target in cancer therapy: a clearer perspective. Eur J Clin Invest 1999;29:733–736.
3. Kerbel RS. Tumor angiogenesis. N Engl J Med 2008;358:2039–2049.
4. Leighl NB, Paz-Arez L, Douillard JL, *et al.* Randomized phase III study of matrix metalloproteinase inhibitor BMS-275291 in combination with paclitaxel and carboplatin in advanced nonsmall-cell lung cancer: National Cancer Institute of Canada-Clinical Trials Group Study BR. 18. J Clin Oncol 2005;23:2831–2839.
5. Siemann DW, Chaplin DJ, Horsman MR. Vascular-targeting therapies for treatment of malignant disease. Cancer 2004;100:2491–2499.
6. Degner FL, Sutherland RM. Theoretical evaluation of expected changes in oxygenation of tumors associated with different haemoglobin levels. Int J Radiat Oncol Biol Phys 1986;12:1291–1294.
7. Mulrane L, Rexhepaj E, Smart V, *et al.* Creation of a digital slide and tissue microarray resource from a multi-institutional predictive toxicology study in the rat: an initial report from the PredTox group. Exp Toxicol Pathol 2008;60:235–245.
8. Dagnon K, Heudes D, Bernaudin JF, *et al.* Computerized morphometric analysis of microvasculature in non-small cell lung carcinoma. Microvasc Res 2008;75:112–118.
9. Belien JA, Somi S, de Jong JS, *et al.* Fully automated microvessel counting and hot spot selection by image processing of whole tumor sections in invasive breast cancer. J Clin Pathol 1999;52:184–192.
10. Axelsson K, Ljung BM, Moore II DH, *et al.* Tumor angiogenesis as a prognostic assay for invasive ductal breast carcinoma. J Natl Cancer Inst 1995;87:997–1008.
11. Barbareschi M, Weidner N, Gasparini G, *et al.* Microvessel density quantification in breast carcinomas: assessment by light microscopy vs. a computer-aided image analysis system. Appl Immunohistochem 1995;3:75–84.
12. Mandelbrot B. The Fractal Geometry of Nature. Freeman: New York, 1983.
13. Cross SS. Fractals in pathology. J Pathol 1997;182:1–8.
14. Baish JW, Jain RK. Fractals and cancer. Cancer Res 2000;60:3683–3688.
15. Baish JW, Gazit Y, Berk DA, *et al.* Role of tumor vascular architecture in nutrient and drug delivery: an invasion percolation-based network model. Microvasc Res 1996;51:327–346.
16. Sandau K, Kurz H. Measuring fractal dimension and complexity—an alternative approach with an application. J Microsc 1997;186:164–176.
17. Chung HW, Chung HJ. Correspondence re: J. W. Baish and R. K. Jain, Fractals and cancer. Cancer Res 2001;61:8347–8350.
18. Masters BR. Fractal analysis of normal human retinal blood vessels. Fractals 1994;2:103–110.
19. Serra J. Biomedical image analysis by mathematical morphology. Pathol Biol (Paris) 1979;27:205–207.
20. Serra J. Image Analysis and Mathematical Morphology. Academic Press: NewYork, 1983.
21. Scott W, Carter C, Lynch M, *et al.* Discovery and development of sorafenib: a multikinase inhibitor for treating cancer. Nat Rev Drug Discov 2006;5:835–844.
22. Rybak JN, Ettorre A, Kaissling B, *et al. In vivo* protein biotinylation for identification of organ-specific antigens accessible from the vasculature. Nat Methods 2005;2:291–298.
23. Chayes F. The Holmes effect and the lower limit of modal analysis. Mineral Mag 1956;31:276–281.
24. Rasband WS, Image J, US National Institutes of Health, Bethesda, MD, USA, http://rsb.info.nih.gov/ij/, 1997–2008.
25. Mann HB, Whitney DR. On a test of whether one of two random variables is stochastically larger than the other. Ann Math Statist 1947;18:50–60.
26. Grizzi F, Russo C, Colombo P, *et al.* Quantitative evaluation and modeling of two-dimensional neovascular network complexity: the surface fractal dimension. BMC Cancer 2005;5:14–22.
27. Bouligand C. Sur la notion d'ordre de mesure d'un ensemble plan. Bull Sci Math 1929;2:185–192.
28. Zhou YJ, Wang SQ, Zhang J, *et al.* A novel method to isolate and map endothelial membrane proteins from pulmonary vasculature. Am J Physiol 2005;288:C950–C956.
29. McDonald DM, Choyke PL. Imaging of angiogenesis: from microscope to clinic. Nat Med 2003;9:713–725.
30. Smith AR. Color gamut transform Pairs. Comput Graph (ACM) 1978;12:12–19. doi:10.1145/965139.807361.
31. MacGillivray TJ, Patton N. A reliability study of fractal analysis of the skeletonised vascular network using the 'box-counting' technique. Conf Proc IEEE Eng Med Biol Soc 2006;1:4445–4448.
32. Siemann DW, Bibby MC, Dark GG, *et al.* Differentiation and definition of vascular-targeted therapies. Clin Cancer Res 2005;11: 416–420.
33. Crohn BB, Ginzburg L, Oppenheimer GD. Regional ileitis. J Am Med Assoc 1932;99:1323–1329.
34. Podolsky DK. Inflammatory bowel disease (1). N Engl J Med 1991;325:928–937.
35. Stefanelli T, Malesci A, Repici A, *et al.* New insights into inflammatory bowel disease pathophysiology: paving the way for novel therapeutic targets. Curr Drug Targets 2008;9:413–418.
36. Deban L, Correale C, Vetrano S, *et al.* Multiple pathogenic role of microvasculature in inflammatory bowel disease: a jack of all trades. Am J Pathol 2008;172:1457–1466.